Tropical Atlantic sea surface temperature and heat flux simulations in a coupled GCM

Léo Siqueira[1] and Paulo Nobre[1]

Received 4 April 2006; revised 5 June 2006; accepted 12 June 2006; published XX Month 2006.

[1] This paper contrasts the SST and heat flux errors in the Tropical Atlantic simulated by the CPTEC Coupled ocean-atmosphere General Circulation Model and its oceanic model forced by momentum and heat estimates. Comparisons between solar radiation estimated by satellite and measurements of PIRATA buoys have been made with the purpose of analyzing the impact of solar radiation in the simulation of SST in the tropical Atlantic. The radiative transfer model (ISCCP DX) has shown higher correlation with the buoys data than ECMWF ERA40 with larger differences over the eastern tropical Atlantic, where the numerical prediction models present difficulties in simulating the appearance of stratus clouds. The use of solar radiation based on satellite estimates and parameterized heat flux generated the best SST and surface heat fluxes. The stronger surface stresses generated by the CGCM contributed to generating an oceanic thermal structure in closer agreement with observations than the OGCM runs. **Citation:** Siqueira, L., and P. Nobre (2006), Tropical Atlantic sea surface temperature and heat flux simulations in a coupled GCM, *Geophys. Res. Lett.*, *33*, LXXXXX, doi:10.1029/2006GL026528.

1. Introduction

[2] Sea Surface Temperature (SST) in the tropical oceans are influenced by the heat flux across the ocean surface, horizontal advection, upwelling, and mixing processes. A change in the balance among these processes causes SST variations, that on interannual and seasonal time scales reflect profound changes in the circulation of the entire tropical oceans [*Philander*, 1990]. The seasonal cycle of the atmosphere-ocean system is determined by complex interactions and feedbacks between elements of the system. Many ocean properties show strong links to overlying atmospheric variability, suggesting that much of the observed ocean variability is driven by the atmosphere.

[3] The amplitude of the tropical Atlantic SST annual cycle is almost an order of magnitude larger than SST interannual variability [*Merle and Hisard*, 1980], suggesting that the later might depend on SST annual cycle. On the other hand, the simulation of SST annual cycle by a coupled ocean-atmosphere GCM (CGCM) is sensitive to the strength/deficiencies of the CGCM's component models. Therefore, understanding these sensitivities is useful to achieve further insight into mechanisms at work for ocean-atmosphere interactions.

[1] Centro de Previsão de Tempo e Estudos Climáticos/Instituto Nacional de Pesquisas Espacias, Cachoeira Paulista, Brazil.

0094-8276/06/2006GL026528$05.00

[4] A possible way to look into the sensitivities of the coupled system is to compare simulations performed by a CGCM and by its oceanic component model (OGCM) forced by observational estimates of heat and momentum fluxes. This study presents such a comparison in the context of the annual evolution of SST and surface heat flux simulated by the CPTEC CGCM and its OGCM (GFDL Modular Ocean Model version 3). Section 2 describes the models used, simulations performed, and data sets used for forcing the OGCM and for model validation. Section 3 compares the annual mean evolution of surface heat flux and SST produced by the CGCM, OGCM, and observational estimates. Section 4 focuses on the temporal evolution of SST and surface heat flux simulations on specific locations. Section 5 summarizes the results and conclusions.

2. Models, Simulations, and Data Sets

[5] The CGCM used in this study consists of a low resolution version of the CPTEC/COLA Global AGCM [*Cavalcanti et al.*, 2002] coupled to GFDL's MOM3 OGCM. The AGCM has 28 layers in the vertical (with top at 50mb) and triangular horizontal truncation at wave number 42, which corresponds to a horizontal resolution of $2.815° \times 2.815°$ (T42L28).

[6] The ocean model used in the CPTEC CGCM is the Modular Ocean Model (MOM) version 3 [*Pacanowski and Griffies*, 1998], from the Geophysical Fluid Dynamics Laboratory (GFDL) where global tropical oceans were considered, with the ocean basins limited at 40°N and 40°S. For the vertical resolution, 20 levels were adopted, 7 of them in the first 100m, spaced by 15m. The longitudinal resolution is 1.5°, and the latitudinal resolution varies gradually from $^1/_2°$ between 10°S and 10°N to almost 3° at 40°S and 40°N. The coupling area is the global tropics, between 40°S and 40°N.

[7] Model's results intercomparison were conducted for the year 1998 only, due to limitations in the solar radiation data set estimated by satellite imagery available at the time of this research. Therefore "Root Mean Squared Errors" (RMSE) presented throughout this article are calculated for 12 monthly values for 1998. A set of three numerical simulations was performed: one coupled CGCM run and two uncoupled OGCM runs. The initial conditions for the two OGCM simulations are taken from a 30 years long OGCM integration (1969–1998) forced by ECMWF ERA40 wind stress, climatological solar radiation [*Oberhuber*, 1988], and surface heat fluxes parameterized following *Rosati and Miyakoda* [1988]. After the spin-up process, two OGCM forced runs were made during the year 1998, both of which used ECMWF ERA40 wind forcing: one used solar radiation fields estimated from satellite

Table 1. Standard Deviation, Mean Error and Correlation Coefficients, for 5 PIRATA Buoy Locations

PIRATA Buoy	PIRATA Std. Dev.	ISCCP Std. Dev.	ERA40 Std. Dev.	ISCCP Mean Error	ERA40 Mean Error	ISCCP CC	ERA40 CC
15°N38W	50.59	53.81	48.94	52.11	10.77	0.89	0.67
8°N38°W	56.19	67.73	68.57	57.31	−5.71	0.87	0.51
0°N35°W	48.18	52.56	47.38	36.37	−27.98	0.90	0.57
0°N0°E	42.04	47.41	54.77	57.14	−25.23	0.81	0.25
10°S10°W	52.04	49.36	36.24	39.09	9.4	0.80	0.4

imagery (ISCCP DX) [*Rossow and Zhang*, 1995; *Pinker et al.*, 1995] and parameterized surface heat flux following *Rosati and Miyakoda* [1988], and the other used total surface heat flux fields from ECMWF ERA40 reanalysis.

[8] The coupled simulation started in December 1997 from the same oceanic IC as the forced OGCM runs and atmospheric IC from CPTEC AGCM forced by observed global SST. During the coupled simulation, observed global SSTs were used poleward of the coupling region.

[9] The verification data sets for surface flux are derived from the Comprehensive Ocean Data set (COADS), $2° \times 2°$ spatial resolution and the in situ data sets from 9 PIRATA buoys. The SST verification data set corresponds to the monthly fields analyzed from the NOAA Optimum Interpolation Sea Surface Temperature Analysis project [*Reynolds et al.*, 2002].

3. Simulations of Surface Heat Flux and SST

[10] The standard deviation, mean error, and correlation coefficients for 5 PIRATA buoy locations were computed and are presented in Table 1 in order to quantify the differences between the solar radiation fields used to force the two OGCM simulations. The higher correlation of ISCCP data with the PIRATA observations is partly due to the higher spacial resolution of the ISCCP solar radiation field. Yet, such correlation differences between the ISCCP and ERA40 solar radiation fields are larger over the eastern tropical Atlantic, where the numerical prediction models present difficulties in simulating the appearance of stratus clouds over cold waters.

[11] Figure 1 shows the net surface heat flux RMSE for the three simulations. The OGCM simulation produces the largest net heat flux errors in the northern and southeastern tropical Atlantic basin when using reanalysis fields (Figure 1a). The OGCM RMSE when using de satellite estimates of solar radiation (Figure 1b) presents comparably smaller magnitudes than the other two simulations shown in Figure 1, mainly over the regions mentioned above. The CGCM (Figure 1c) shows RMSE spatial distribution similar to the OGCM forced by reanalysis fields (Figure 1a), except over the northern tropical Atlantic, were the CGCM RMSE are smaller, and off the cost of Guinea where CGCM RMSE are larger. As the next section will show, the major contributions to the RMSE shown in Figure 1 are deficiencies in the latent and radiative fluxes; sensible heat flux (figures not shown) are important only at higher latitudes and will not be discussed further.

[12] The comparison between the surface solar radiation RMSE fields for the ECMWF ERA40 and CPTEC CGCM relative to the ISCCP estimates (Figure 2) shows that both RMSE fields are of the same order of magnitude, with the ERA40's errors (Figure 2a) generally higher than CPTEC's.

[13] Figure 3 shows latent heat RMSE maps for the two OGCM and the coupled simulations. It is noteworthy in Figure 3 that the smallest latent heat RMSE values are found for the OGCM simulation forced with ISCCP solar radiation (Figure 3b). Both OGCM ERA40 and CGCM latent heat RMSE fields present the same order of magnitude, with the exception of the larger CGCM errors over the northern subtropics and equatorial Atlantic (Figures 3a and 3c). The combination of the large evaporative and solar flux errors over the northern tropical Atlantic and southeastern equatorial Atlantic (Figures 3a and 3c and Figures 2a and 2b respectively) suggest that these are the main contributors to the errors in the net surface heat flux shown in Figure 1a and 1c.

[14] Figure 4 shows the SST RMSE for the three simulations performed. The net heat flux errors over the northern tropical Atlantic and eastern equatorial Atlantic causes the largest SST errors over these regions for the OGCM simulation using ERA40 fields (Figure 4a). The reduced errors in SST are noteworthy in Figure 4b, when forcing the

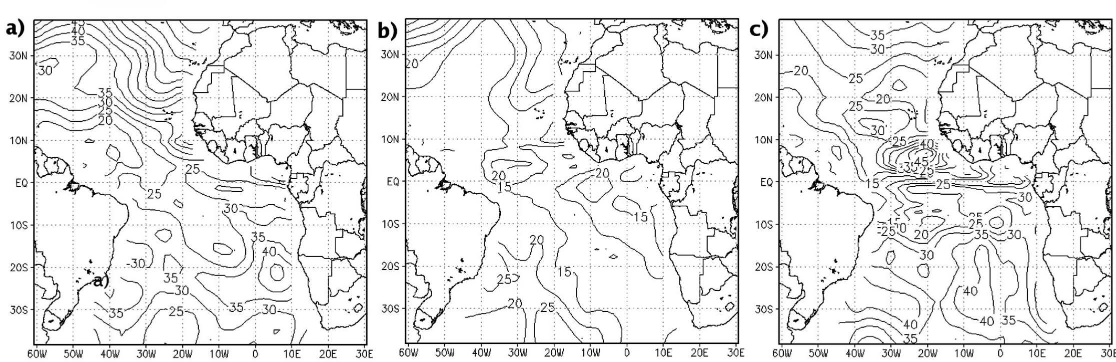

Figure 1. Net surface heat flux RMSE (Wm^{-2}): (a) ECMWF ERA40; (b) ISCCP DX; (c) CPTEC CGCM.

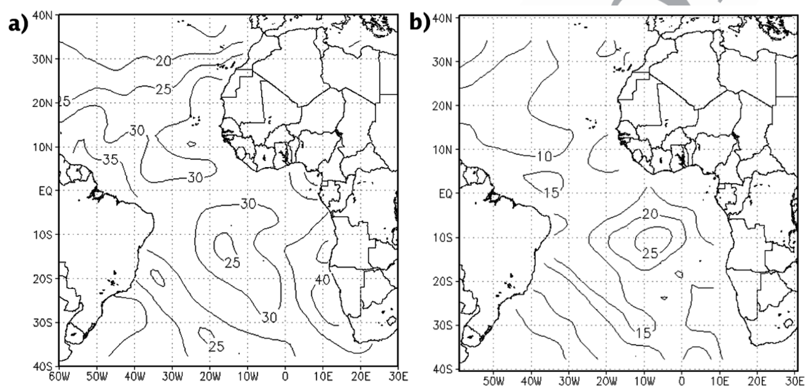

Figure 2. Surface solar radiation RMSE (Wm^{-2}): (a) ECMWF ERA40; (b) CPTEC CGCM.

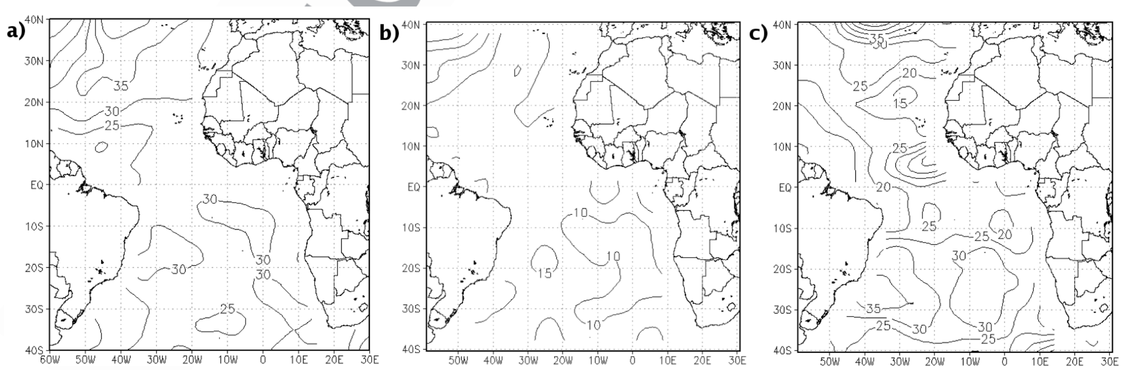

Figure 3. Surface latent heat RMSE (Wm^{-2}): (a) ECMWF ERA40; (b) ISCCP DX; (c) CPTEC CGCM.

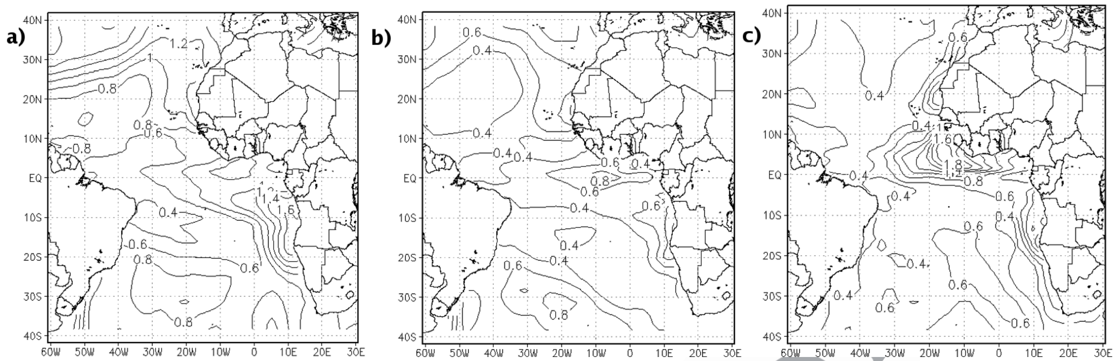

Figure 4. SST RMSE (°C): (a) ECMWF ERA40; (b) ISCCP DX; (c) CPTEC CGCM.

OGCM with solar radiation fields computed from satellite estimates and parameterized latent, longwave, and sensible heat fluxes. This simulation shows a strong error reduction over the northern tropical and eastern equatorial Atlantic. The CPTEC CGCM (Figure 4c) presents a similar error pattern of that in the OGCM simulation forced by satellite estimates (Figure 4b), except over the central basin where the larger CGCM errors in latent heat loss (Figure 3c) contributes to the large magnitudes in the SST errors shown in Figure 4c.

[15] The main results of the three numerical simulations are summarized in Table 2, in the form of RMSE spatial mean over the entire tropical Atlantic. Overall, the main contributors for the net heat flux errors in the presented simulations are the shortwave and latent heat for all simulations (Table 2). Accordingly, OGCM simulations showed the best overall results when surface heat fluxes are parameterized, but the solar fluxes are estimates derived from satellite IR imagery. Surprisingly, CGCM heat fluxes errors are only “marginally” larger than the ISCCP forced OGCM simulation (with the exception to the latent heat, for which the OGCM ERA40 simulation shows smaller mean error); while the ERA40 forced OGCM simulation presents the largest errors. Here, two processes might be at play; one is the expected improvement of simulated surface heat fluxes due to the presumably better estimate of shortwave solar radiation inferred from satellite IR data, as compared with the ERA40’s solar fluxes. The other is the possibility that surface momentum fluxes from the ERA40 reanalysis are worse than the CGCM stresses, thus impacting in the wind-induced evaporation and equatorial upwelling. Figure 5a shows a longitude-depth cross section of the second derivative of temperature with depth along the equatorial Atlantic (as an estimate of thermocline slope and depth) for the three numerical experiments and Levitus climatology [*Levitus and Boyer*, 1994].

[16] It is remarkable to observe in Figure 5a that the CGCM thermocline is shallower in the east and presents a steeper east-west inclination than the thermoclines of both OGCM forced runs. This is an indication that the surface stress product generated by the CGCM is likely to be more energetic than the ERA40 stress products in the equatorial area, where the coupling is stronger. Such supposition is confirmed by the annual mean difference stress field shown in Figure 5b, confirming our supposition that ERA40 stresses are too weak, resulting both; an excessively flat thermocline and less evaporative cooling of surface waters. The root of such deficiencies might be in the very nature of two-tier approach of reanalysis. In regions like the eastern equatorial Atlantic, where stratus cloud decks form over cool waters, the reanalysis process uses observed SST, and generally produces subsidence that may not occur over these regions, increasing the solar flux and consequently, in our numerical experiments, the SST, which leads to greater surface flux errors.

[17] Heat transport mechanisms in the equatorial region, such as vertical entrainment, zonal and meridional heat advection also play an important role in the SST’s determination. In order to access to what degree such transport mechanisms contribute to the mean error fields shown above, the zonal, meridional, and vertical heat transport differences between CGCM and OGCM-ERA40 simulations are computed following the heat storage rate equation in the work by *Moisan and Niiler* [1998], and shown in Figure 6. The examination of these components of the heat transport over the equatorial Atlantic reveals strong differences between the CGCM and the OGCM simulations in the zonal advection and vertical entrainment (Figures 6a and 6c). The greater magnitudes of CGCMs westward zonal heat advection in the central portion of the equatorial Atlantic together with the stronger vertical entrainment in the central and eastern portion indicates that the CGCM ocean dynamics promotes a better representation of the thermocline slope and depth due to the greater mixed layer heat loss provided by these two process.

4. Seasonal Cycle at Specific Locations

[18] To quantify the time evolution of the RMSE fields shown in the previous section, time series at two PIRATA sites are examined with respect to the seasonal evolution. The chosen points are at 15°N, 38°W and at 0°N, 0°E, because of the differences in ocean dynamics and atmo-

Table 2. RMSE Spatial Mean: SST and Heat Flux Components

	Era40	ISCCP	CPTEC CGCM T42L28
SST	0.89	0.52	0.53
Net heat flux	33.81	17.53	27.90
Short wave	31.79	13.76	19.45
Latent heat	28.72	19.08	34.35
Sensible heat	8.12	5.03	5.4
Long wave	6.40	8.21	5.93

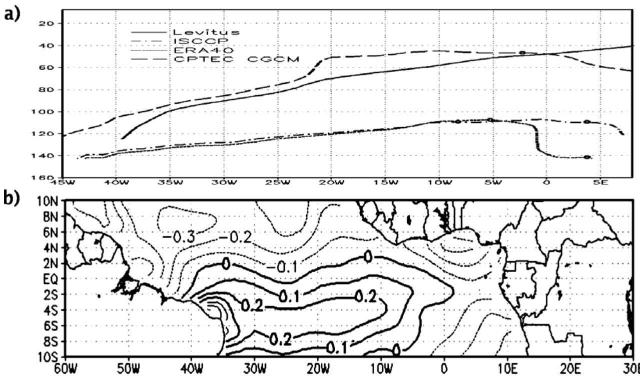

Figure 5. (a) Longitude-depth cross section of maxima temperature vertical gradient along the equator (as an indication of the positioning of the thermocline) for both OGCM forced runs (dash-dotted and dotted lines) and for the CGCM run (thick dashed line), and Levitus climatology (thick continuous line). (b) Annual mean difference CGCM – ERA40 wind stresses (dynes/cm^2).

spheric forcing between these two locations. The seasonal evolution for monthly averages for SST, net heat, solar, and latent heat fluxes are shown in Figure 7.

[19] The CGCM seasonal evolution of SST at 15°N, 38°W (Figure 7a) presents the best resemblance with the PIRATA observations of all simulations, albeit the general bias of all simulations (see RMSE values on the panels of Figure 7). On the other hand, the SST simulations at 0°N, 0°E (Figure 7b) show a discrepant behavior related to the observations, as both the CGCM and the ocean simulation forced by reanalysis fields were unable to represent both the

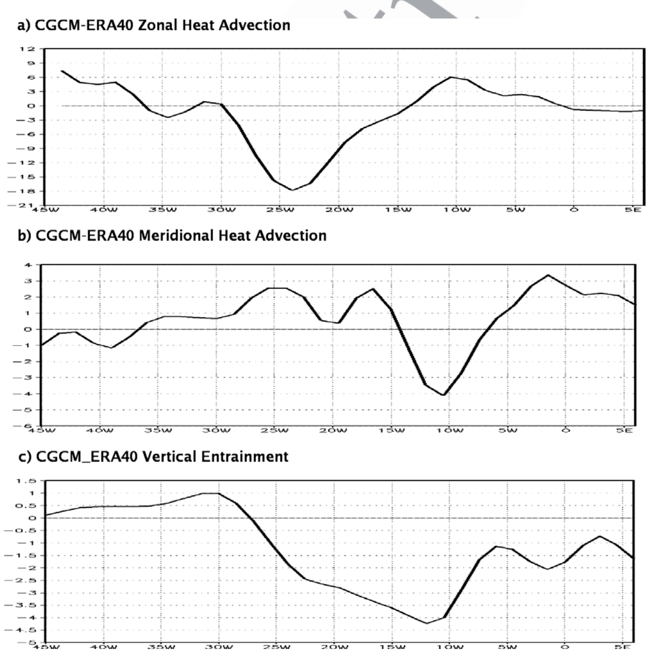

Figure 6. Longitudinal cross section at 0°N of annual mean difference: (a) CGCM-ERA40 Zonal Advection (W/m^2); (b) CGCM-ERA40 Meridional Advection (W/m^2); (c) CGCM-ERA40 Entrainment (W/m^2).

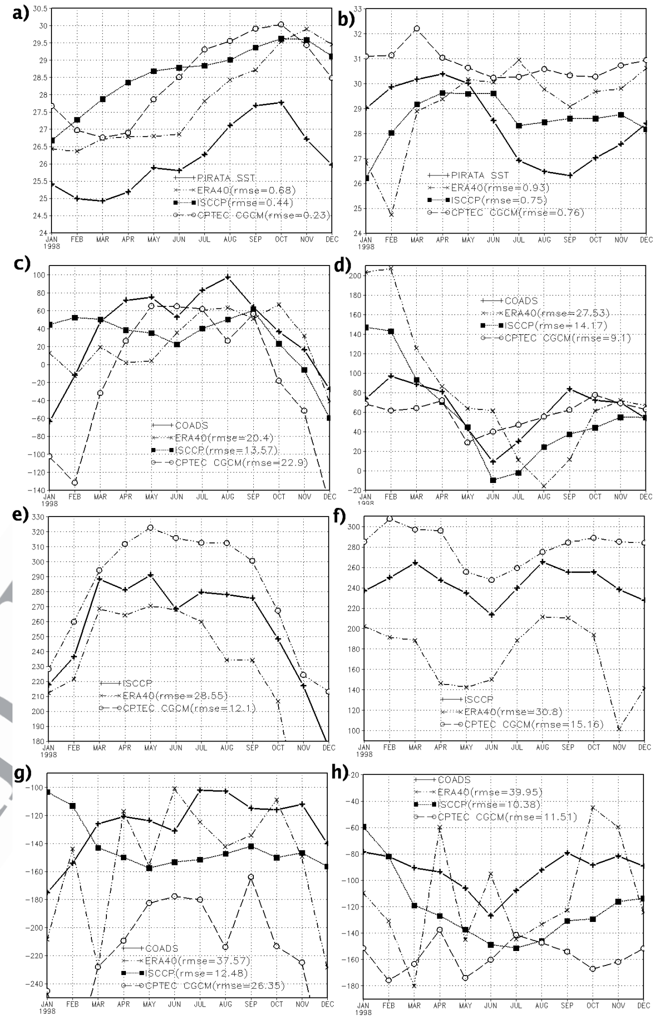

Figure 7. (a and b) Time series of SST (°C); (c and d) net heat (Wm^{-2}); (e and f) solar heat (Wm^{-2}); and (g and h) latent heat (Wm^{-2}) at the PIRATA sites 15°N, 38°W (left column) and 0°N, 0°E (right column), respectively.

amplitude and phase of the observed SST time evolution at this site.

[20] The annual march of the net heat flux (Figures 7c and 7d) simulations show smaller discrepancies with observations than the simulated latent heat loss, shown in Figures 7g and 7f. The smaller discrepancies of the net heat fluxes indicate that compensation between the solar and latent heat are in place, as it can be verified by comparison of Figures 7e and 7g and Figures 7f and 7h over both PIRATA sites. The positive CGCM bias of solar heating is partially offset by the larger evaporative cooling bias. Such compensation is not so evident for the ERA40 simulation, resulting the larger discrepancies of the OGCM simulations shown in Figures 7c and 7d.

5. Discussion

[21] In this work comparisons have been made between two surface solar radiation products with in situ measurements of the PIRATA buoys, with the purpose to analyze the impact of solar radiation fluxes estimated by different

methods and heat flux parameterization in determining SST variations in the tropical Atlantic.

[22] The radiative transfer model (ISCCP DX - NOAA/NASA PATHFINDER) has shown higher correlation with the buoys data than ECMWF ERA40 fields. The differences are larger in regions where the numerical prediction models shows difficulties in simulating the appearance of stratus clouds over cold waters such as the eastern equatorial Atlantic.

[23] Two oceanic simulations forced with estimates of solar heat and momentum fluxes and a coupled ocean-atmosphere simulation were done. Based on the simulations results with different solar radiation inputs and heat flux parameterization, significant differences in SST and heat flux fields were detected suggesting that solar heat flux is of primordial importance to reduce SST errors on forced model simulations.

[24] The use of solar radiation fields based on satellite estimates and parameterized heat flux generated the best SST and surface heat fluxes simulations. The CGCM SST simulations were second best, due in part to latent and solar heat fluxes bias compensation, and in part to its better oceanic thermal structure. The examination of the oceanic heat transport over the equatorial Atlantic revealed strong differences between the CGCM and the OGCM forced runs. The surface stress generated by the CGCM has shown to be more energetic in the equatorial area than the ERA40 reanalyses. The stronger surface stresses generated by the CGCM contributed to generating an oceanic thermal structure in closer agreement with observations, thus suggesting the importance of the wind stress quality to correctly simulate oceanic advection and evaporative processes.

[25] The validation of the model results still requires systematic comparisons for longer periods of time. To validate the CGCM results against observation is a necessary task, and it is part of our current research undertakings.

[26] **Acknowledgments.** The authors acknowledge R. Pinker for the solar radiation data and Marta Malagutti and Emanuel Giarolla for their help with the modelling work. This work is a result of the first author's Master Thesis at INPE, and was partially funded by a grant from CAPES and CNPq.

References

Cavalcanti, I. F. A., et al. (2002), Global climatological features in a simulation using the CPTEC–COLA AGCM, *J. Clim.*, *15*, 2965–2988.

Levitus, S., and T. Boyer (1994), *World Ocean Atlas 1994*, vol. 4, *Temperature*, *NOAA Atlas NESDIS 4*, U.S. Dep. of Commer., Washington, D. C.

Merle, J. P., and P. Hisard (1980), Annual signal and interannual anomalies of sea surface temperature in the eastern equatorial Atlantic Ocean, *Deep Sea Res.*, *26*, 77–101.

Moisan, J. R., and P. P. Niiler (1998), The seasonal heat budget of the North Pacific: Net heat flux and heat storage rates (1950–1990), *J. Phys. Oceanogr.*, *28*, 401–421.

Oberhuber, J. M. (1988), An atlas based on "COADS" data set, *Tech. Rep. 15*, Max-Planck-Inst. für Meteorol., Hamburg, Germany.

Pacanowski, R. C., and S. M. Griffies (1998), MOM 3.0 manual, NOAA/Geophys. Fluid Dyn. Lab., Princeton, N. J.

Philander, S. H. G. (1990), *El Niño, La Niña, and Southern Oscillation*, 293 pp., Elsevier, New York.

Pinker, R. T., et al. (1995), First global WCRP shortwave surface radiation budget dataset, *Bull. Am. Meteorol. Soc.*, *76*, 905–922.

Reynolds, R. W., N. A. Rayner, T. M. Smith, D. C. Stokes, and W. Wang (2002), An improved in situ and satellite SST analysis for climate, *J. Clim.*, *15*, 1609–1625.

Rosati, A., and K. Miyakoda (1988), A general circulation model for upper ocean simulation, *J. Phys. Oceanogr.*, *18*, 1601–1626.

Rossow, W. B., and Y. C. Zhang (1995), Calculation of surface and top-of-atmosphere radiative fluxes from physical quantities based on ISCCP datasets, part II: Validation and first results, *J. Geophys. Res.*, *100*, 1167–1197.

P. Nobre and L. Siqueira, Centro de Previsão de Tempo e Estudos Climáticos/Instituto Nacional de Pesquisas Espacias, Rod. Pres. Dutra, Km 40, 12630-000, Cachoeira Paulista, SP, Brazil. (leosan@cptec.inpe.br)